RSC Advances

PAPER

View Article Online
View Journal | View Issue

Cite this: *RSC Adv.*, 2017, **7**, 41217

Mutual-stabilization in chemically bonded graphene oxide–TiO_2 heterostructures synthesized by a sol–gel approach

Usuma Naknikham,[a] Vittorio Boffa,*[a] Giuliana Magnacca,[b] Ang Qiao,[c] Lars Rosgaard Jensen[d] and Yuanzheng Yue*[ac]

Received 8th July 2017
Accepted 16th August 2017

DOI: 10.1039/c7ra07472g

rsc.li/rsc-advances

We study the structure of the photocatalytic graphene oxide–titanium dioxide (GO–TiO_2) nanocomposites prepared by *in situ* sol–gel nucleation and growth of TiO_2 on GO sheets. Fourier transform-infrared (FTIR) and X-ray photoelectron (XPS) spectra of these composites indicate that the GO sheets and the TiO_2 nanoparticles interact through Ti–O–C bonds. This chemical interaction is strong enough to ensure mutual stabilization during thermal annealing, and thereby GO inhibits TiO_2 crystallization. In addition, thermal reduction of GO nanoribbons anchored to TiO_2 nanoparticles occurs at a higher temperature and with a lower released energy than in the pure GO powder. Understanding of the mutual-stabilization mechanisms is critical for the rational design of GO–TiO_2 photocatalysts.

1. Introduction

The breakthroughs of graphene research have been revolutionizing many research fields owing to the superior physical and chemical properties of graphene-based materials over a broad application spectrum.[1–3] For instance, graphene–TiO_2 heterostructures have opened a new direction in the development of heterogeneous photocatalysts for environmental applications.[4–6] Nowadays, the benchmark material for photocatalytic application is TiO_2, because it is inexpensive, chemically inert and has high photocatalytic activity in the abatement of organic pollutants.[7] However, the TiO_2 efficiency is limited by high rate of electron–hole pair recombination and its band-gap can only be used to exploit UV-light.[8–10] In principle, the combination of TiO_2 and graphene allows for superior photocatalytic properties, because graphene can potentially act as electron acceptor for hindering electron–hole recombination and it can increase the absorption range from UV to visible light of TiO_2.[7,10,11] In addition, graphene can function as an absorbant,[12] thus holding pollutants close to the TiO_2 photocatalytic centers.[2]

TiO_2–graphene photocatalysts have recently attracted considerable interest and different methods have been established for their fabrication. Such methods often involve the synthesis or the deposition of TiO_2 nanoparticles on water dispersed graphene oxide (GO) sheets. Indeed, the use of GO offers several advantages, because GO can be easily prepared by chemical oxidation and exfoliation of natural graphite,[2,13] it can be easily dispersed in water, and it can subsequently be thermally or chemically reduced to graphene-like structures (rGO).[12,14] Furthermore, in such heterostructures the interactions between GO functional groups and the surface of the nanoparticles are beneficial for integrating the respective merits and to solve compatibility problems during synthesis and post-treatment, thus yielding composites with enhanced properties.[15,16]

TiO_2–rGO composites prepared by hydrothermal and solvothermal processes exhibit good chemical bonding at the interface.[8,17] However, these methods work for specific conditions and equipment, *e.g.*, in the cases of high temperature, Teflon autoclave or organic solvents.[8,17,18] On the contrary, the sol–gel synthesis is simple, requires mild conditions, and makes it possible to obtain narrow size distributions in the nanometer range.[19] In addition, controlling pH offers the possibility to exploit the strong electrostatic interaction between the negative charged GO sheets and the positively charged surface of TiO_2 nanoparticles.[11,19] For instance, Zhang *et al.* succeeded in synthesis of a GO–TiO_2 intercalated composite by electrostatic attraction *via* a sol–gel process at 80 °C.[20] $[TiO]^{2+}$ was introduced into GO interlayer exfoliated in 0.2 M NaOH, so that the nucleation and growth of TiO_2 crystal occurred *in situ*. The photo-degradation of methyl orange solution under UV light of this GO–TiO_2 composite within 15 minutes (87.2%) was stronger than that of the reference Degussa P25 powder (38.4%). The interaction between GO and TiO_2 nanoparticles can also be used to prepare stacked graphene membranes with photocatalytic properties,[21–24] where the

[a]*Department of Chemistry and Bioscience, Aalborg University, 9220 Aalborg, Denmark. E-mail: vb@bio.aau.dk; yy@bio.aau.dk*

[b]*Dipartimento di Chimica, NIS Centre, Universitá di Torino, 10125 Torino, Italy*

[c]*State Key Laboratory of Silicate Materials for Architectures, Wuhan University of Technology, Wuhan 430070, China*

[d]*Department of Materials and Production, Aalborg University, 9220 Aalborg, Denmark*

oxygen functional groups on GO interact with graphene sheets forming interlocked layers.[25] Based on these heterostructures, the size of the TiO_2 nanoparticles can be used to tune the space between GO layers and hence to control the membrane permselectivity.[26] On the other hand, synthesis parameters can affect the morphology of titanium dioxide nanoparticles and the density of oxygen moieties on GO sheets, and hence, the photocatalytic performance and the processability of these materials. For instance, Lambert *et al.* prepared paper-like GO–TiO_2 composites *via* hydrolysis of TiF_4 at 60 °C for 24 hours.[27] These composites showed the co-existence of highly oxidized graphene and TiO_2 nanocrystals with anatase phase.

In this context, it is important to investigate how TiO_2 nanoparticles and GO sheets can mutually influence their morphological evolution during synthesis and during thermal annealing. In a recent paper, Boffa *et al.* have demonstrated the ability of a waste-derived biopolymer, with functional group distribution similar to GO, to control the morphology of TiO_2 nanoparticle during sol–gel synthesis.[28] Therefore, we expect that the presence of GO will influence the formation and the growth of TiO_2 nanoparticles during synthesis. In this work, TiO_2 nanoparticles were synthetized *via* the sol–gel method, in the presence of GO sheets. pH was kept at 6 in all the syntheses, while synthesis temperature ranged between 60 °C to 100 °C. No synthesis above 100 °C was performed, to preserve the functional groups on graphene oxide,[29] an important structural feature for the fabrication of photocatalytic membranes for the degradation water pollutants under the visible light. Moreover, this gave the opportunity to further investigate the behavior of such groups during thermal annealing. The loading of GO in the nanostructured materials was varied from 0 to 50 wt%, to study the concentration effect. All the syntheses were performed in 4 hours, except for one sample with 1 wt% GO loading, which was prepared in 24 hours at 100 °C. Thus, it was also possible to investigate the structural evolution of the materials for a long aging time.

2. Experimental section

2.1 GO preparation

All the chemicals used for the synthesis of the nanocomposites were purchased from Sigma-Aldrich, unless otherwise specified. GO was prepared *via* a modified Hummers methods.[30] 2.0 g natural graphite powder (Graphit Kropfmühl GmbH) was dispersed in concentrated H_2SO_4 solution (50 mL, 98%) in an ice bath. Then, 6.0 g potassium permanganate ($KMnO_4$) was slowly added and the mixture was heated at 35 °C in an oil bath for 2 hours. After that, the suspension was cooled in an ice bath and 350 mL deionized water (DI) were slowly added. H_2O_2 solution (30%) was slowly dropped into the mixture until gas development stopped and the suspension became orange-yellow. All steps were done under continuous vigorous stirring. The precipitate was washed with DI water until pH of the supernatant become natural and was then freeze-dried to obtain a graphite oxide powder, which can be easily dispersed in water.

2.2 Synthesis of the GO–TiO_2 composites

TiO_2 photocatalysts with theoretical GO loading of 0, 1 and 50 wt%, named T-4, 1GT-4 and 50GT-4, respectively, were synthesized. The ratios of $TiCl_4$/GO/H_2O in the synthetic mixtures were adjusted to obtain the desired GO loading and a total GO + TiO_2 concentration of 2.5 g L^{-1}. Firstly, graphite oxide powder was dispersed in 100 mL ultrapure water (resistivity $\geq$ 18 MΩ cm) in an ultrasonic bath for 30 minutes. After that, the suspension was stirred in an ice bath for 30 minutes. $TiCl_4$ (98%) was added and stirred at 600 rpm for an hour, while heating was avoided by keeping the mixture in the ice bath. Then, the suspension was let to reach room temperature (~22 °C) and the pH was adjusted with NH_4OH solution (25%) to 6. pH was maintained at 6 for 2 hours, and then the mixture was heated at the target temperature of the synthesis in an oil bath for 4 hours under vigorous stirring. Synthesis temperatures ranged between 60 °C and 100 °C, as specified for each sample in the Results and discussion section. For one sample with 1 wt% GO loading, namely 1GT-24, the temperature was maintained at 100 °C for 24 hours. After synthesis, the suspensions were left to cool to reach room temperature while continuously stirring for 18 hours. After this, TiO_2–GO nanocomposites were collected by centrifugation and cleaned with DI water until the silver nitrate test (0.1 M $AgNO_3$ solution) on the washing solution was negative, *i.e.* no chloride ions were detected. Finally, the precipitation was washed with ethanol and dried in vacuum at 40 °C.

2.3 Characterization of the GO–TiO_2 composites

The structure of the samples was characterized by scanning electron microscope, SEM (Zeiss, 1540 XB). High-resolution transmission electron microscopy (HRTEM) images were obtained with a JEOL 3010-UHR instrument. The crystalline phase and the size of TiO_2 nanoparticles, and the interlayer distance of GO were investigated using a PANanalytical Empyrean diffractometer, operating at 45 kV and 40 mA, with Cu Kα radiation (λ = 1.5418 Å). Both reflection spinner and SAXS stage were used. SAXS measurements were performed over a q interval included between 5.3×10^{-3} $Å^{-1}$ and 3.5×10^{-1} $Å^{-1}$. After background subtraction, the scattered intensity I was plotted as a function of the scattering vector q, and the size distribution of the titania particles was obtained by fitting eqn (1) on the experimental data.

$$I(q,R) \propto \int_0^{R_{max}} D_v(R) R^3 I_p(q,R) dR \quad (1)$$

where $D_v(R)$ refers to the volume-weighted particle size distribution, that is, when $D_v(R)$ is normalized, it indicates the probability of particles having a radius within dR. For homogeneous particles of radius R, the scattering intensity profile, $I_p(q,R)$,[31,32] is known and expressed by eqn (2):

$$I_p(q,R) = K\Delta\rho^2 V_p \left(\frac{\sin(qR) - qR\cos(qR)}{(qR)^3} \right)^2 \quad (2)$$

where R is the particle radius, K is an apparatus-dependent optical constant that is independent of the scattering

produced by the sample, $\Delta\rho$ is the excess electron density of the particle with respect to the surrounding medium, V_p is the volume of the particle. X-rays diffraction (XRD) patterns of the powdered samples were acquired in a 2θ range from 5° to 80°. Reference cards PDF 01-021-1272 of anatase and 01-029-1360 of brookite were chosen for peak analysis.[33] The average size of (101) TiO_2 crystallites and the thickness of the GO domains were calculated by Scherrer equation[34] by using a shape factor (k) of 0.9 and 1.84 for TiO_2 nanoparticles and GO,[35] respectively. The weight fraction of the anatase phase, W_A, over the total crystalline material (anatase and brookite) was calculated by eqn (3).[33,36]

$$W_A = \frac{k_A A_A}{k_A A_A + k_B A_B} \quad (3)$$

where A_A is the integrated intensity of anatase phase highest peak (101), A_B is the integrated intensity of brookite phase highest peak (121), and the coefficients, k_A and k_B are 0.886 and 2.721, respectively. The deconvolution technique was used for anatase and brookite peak separation due to their overlapping. After baseline subtraction, the XRD pattern was fitted by Lorentzian function over the Fityk 0.9.8 software. By doing that, it was assumed that the broadening of the three main peaks of brookite is the same.[33]

Fourier transform-infrared spectroscopy, FTIR (Varian Cary®50 UV-Vis Spectrophotometer), was performed by using the KBr technique (KBr : sample = 100 : 0.1) to investigate which type of functional groups was present in the nanocomposite materials, and the interaction between GO and TiO_2. The measurement was conducted within the wave number interval 400–4000 cm^{-1} in transmittance mode. XPS spectra were obtained by an ESCALAB 250Xi X-ray photoelectron spectrometer (Thermo Fisher Scientific) using Al Kα radiation. RAMAN spectroscopic measurements were performed on an Invia RAMAN microspectrophotometer (Renishaw) in the backscattering geometry with $\lambda = 532$ nm. The thermal evolution of the photocatalysts was determined from 50 to 800 °C by differential scanning calorimetry and thermogravimetry (DSC/TG) over a NETZSCH STA 449 F1 Jupiter, at a heating rate of 10 °C per minute, with platinum crucible, and under argon atmosphere.

3. Results and discussion

3.1 Size and dispersion of TiO_2 nanoparticles

In this section, we present and discuss the structural features of a pure TiO_2 reference sample synthetized in 4 hours (T-4), two TiO_2 nanocomposites with 1 wt% GO loading synthetized in 4 hours and 24 hours (1GT-4 and 1GT-24 respectively), and a TiO_2 nanocomposite with 50 wt% GO loading synthetized in 4 hours (50GT-4). For simplicity, these materials are hereafter referred according to the designations that are reported above.

The morphology of the GO–TiO_2 nanocomposites was investigated by electron microscopy. Fig. 1 shows the SEM images of the starting GO and of 50GT-4. The carbon layers of the starting GO forms an open sponge-like structure (Fig. 1(a)), as typical of freeze-dried GO.[37] 50GT-4 consists of TiO_2 particles with size of a few nanometers, which are packed into large agglomerates, either covering or intercalating GO sheets, thus making GO structures not visible at SEM. No structural differences between the samples prepared in the presence of GO and the pure TiO_2 reference were observed. Therefore, size and dispersion of TiO_2 particles in the GO–TiO_2 nanocomposites were investigated by HR-TEM analysis, as shown in Fig. 2. Fig. 2(a) shows highly agglomerated TiO_2 nanocrystals in the T-4 sample. The high magnification micrograph in Fig. 2(d) confirms that these crystals have size of few nanometers and shows that they have polyhedral shape. Fig. 2(b) shows a micrograph of the 1GT-4 powder. Also in this case, TiO_2 nanocrystals are highly agglomerated; but they anchor over an isolated GO sheet (red arrow) and partially cover it. In the case of the sample prepared with 50 wt% GO loading, namely 50GT-4, TiO_2 nanoparticles are less agglomerated than in the other samples and decorate GO ribbons (Fig. 2(c)). The fingerprint of both TiO_2 and GO ribbons are visible in Fig. 2(f), where we can observe two TiO_2 crystallites (white arrows) laying with one of their facet over a 5–10 nm thick GO ribbons (red circle). Such GO ribbons are typical of GO-based materials,[29] but were not found in the micrographs of 1GT-4 (Fig. 2(b) and (e)). This could be ascribed to the fact that, at low GO loading, TiO_2 nanoparticles can fully intercalate GO sheets (see the red arrow in Fig. 2(b)), thus avoiding the formation of GO nanoribbons. The high magnification micrographs (Fig. 2(d)–(f)) show that all the samples are made of crystalline particles (as evidenced by the presence of interference fringes) with polyhedral shape and size around 7–10 nm.

The size distribution of TiO_2 particles in T-4, 1GT-4, 1GT-24 and 50GT-4 was measured by SAXS. The scattering curves (Fig. 3(a)) were analyzed in terms of size distribution functions, $D_v(R)$, which are depicted in Fig. 3(b). The distribution is in agreement with that of the particles observed at HR-TEM. The particles are smaller than 20 nm with average diameter, d_{SAXS}, ranging between 7.6 and 9.0 nm. Nevertheless, d_{SAXS} of T-4 is 8.6 nm, which is larger than that of the TiO_2 particles prepared in the presence of GO. This can be explained by considering that GO sheets contains a large number of oxygen functional groups which can interact with Ti^{4+} ions and titania cluster. Thus, they act as nucleation sites around which titanium dioxide nanoparticles grow during synthesis.[27,28,38] The presence of a large number of such nucleation sites over GO sheets results in a smaller particle size for 1GT-4 and 50GT-4, compared to T-4. At 1 wt% of GO loading, only after 24 hours of reaction time (1GT-24), TiO_2 particles reach a size comparable to those in the T-4 sample. Surprisingly, 1GT-4 and 50GT-4 have similar particle size distribution with both $d_{SAXS} = 7.6$ nm, suggesting that the GO concentration in the reaction mixture has a negligible impact on the size of TiO_2 nanoparticles. However, this result can be explained by considering: (i) the high density of oxygen functions on the GO sheets, and (ii) the lower exposure of the GO functional groups in the sample prepared with the 50 wt% GO loading. Indeed, as shown by Fig. 2, GO sheets in 1GT-4 are well intercalated by the TiO_2 nanoparticles, while in 50GT-4, GO sheets form staked nanoribbon structures, resulting in a much lower

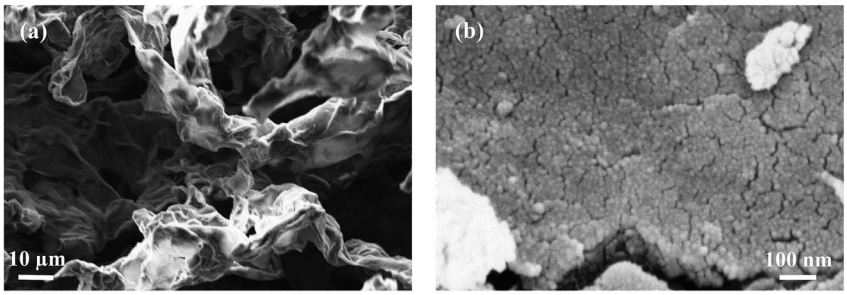

Fig. 1 SEM images of (a) the freeze-dried GO and (b) the nanocomposite prepared with 50 wt% of GO, at 100 °C, for 4 hours (50GT-4).

exposure of the GO functional groups to the interaction with TiO_2 clusters and particles.

3.2 Order/disorder in the TiO_2–GO nanocomposites

The morphology of GO and the composite materials was further investigated by XRD analysis. Fig. 4 shows the XRD patterns of bare GO, pure TiO_2, and TiO_2–GO composites. The starting GO shows a peak at $2\theta = 10.46°$,[39,40] which corresponds to a *d*-space distance of 8.45 Å, and is consistent with the staking of highly oxidized graphene sheets. The characteristic GO peak is not visible in the powders prepared with 1 wt% GO loading. This observation matches with the HR-TEM micrographs of 1GT-4, where no GO layered structure was found, although the presence of such structures cannot be completely excluded. The diffraction is relatively weak because the amount of GO in this material is rather low.[12,41] On the contrary, the characteristic GO peak is clearly visible in the diffractogram of the 50GT-4 powder, indicating restacking of GO layers in this material.[27] However, the peak is broader than the one of the pristine GO and its maximum is shifted towards a higher 2θ value, namely 12.01° (*d*-space = 7.36 Å). As discussed later, a decrease of the interlayer distance is an indication of the partial reduction of the oxygen groups during synthesis. The FWHM (full width at half maximum) of the peaks was used to calculate the thickness of the stacked GO domains by the Scherrer equation. Scherrer distances of 24 nm and 9.2 nm were obtained for the starting GO and 50GT-4, respectively. In the case of 50GT-4, the distance corresponds to staking of about 12.5 GO layers and is consistent with the HR-TEM micrographs reported in Fig. 2(c) and (f). Moreover, TiO_2 nanoparticles are expected to disrupt the parallel stacking of graphene oxide layers, thus resulting in a shorter Scherrer distance for 50GT-4 than for the pristine GO powder. XRD analysis was also used to investigate the crystal structure of TiO_2 nanoparticles in the GO–TiO_2 nanocomposites and in the T-4 reference. All the diffractograms show the characteristic peak of the anatase phase (A) and the peaks of the brookite (B) phase, but with a lower intensity. The average size of the anatase crystallites was calculated from the FWHM of the peak at $2\theta \sim 25.2°$, obtaining the values of 6.4, 6.6, 7.4 and

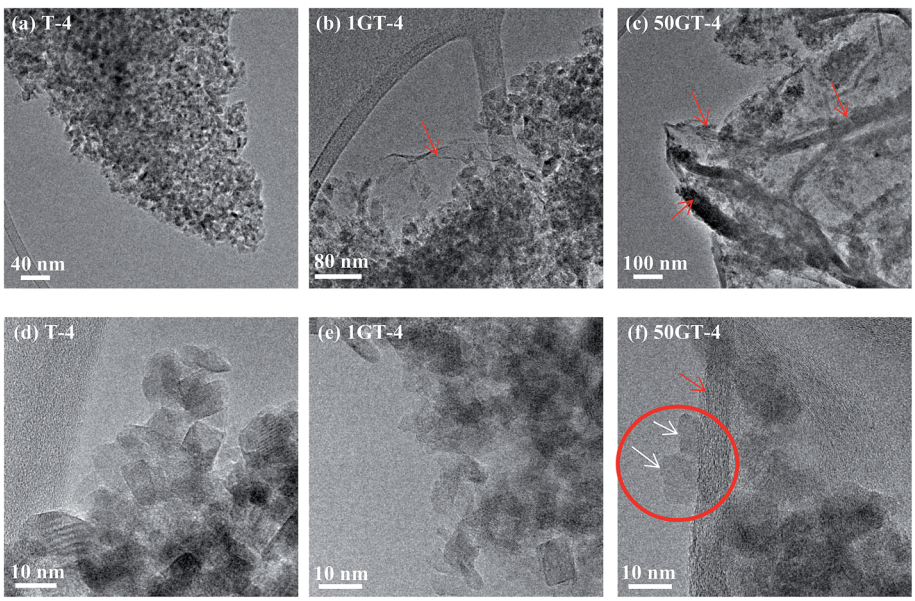

Fig. 2 TEM images of the samples prepared at 100 °C for 4 hours. (a, d) The pure TiO_2 reference (T-4), (b, e) the nanocomposites with 1 wt% GO (1GT-4), and (c, f) the nanocomposite with 50 wt% GO (50GT-4). Pictures were taken at low (first row) and high magnification (second row). The red arrows point at GO sheets and the white arrows point at TiO_2 crystals.

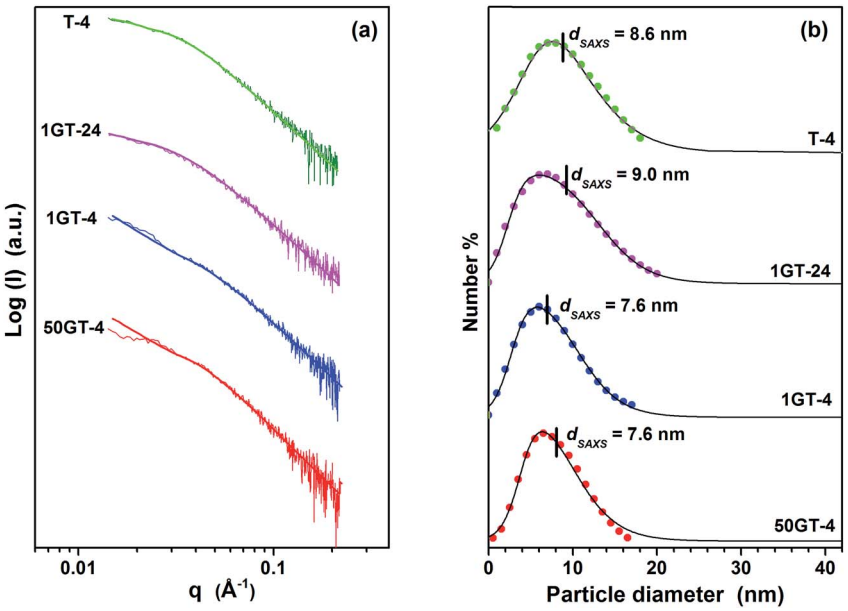

Fig. 3 (a) SAXS curves and (b) correspondent TiO_2 particle size distribution of the GO–TiO_2 composites. The dots indicate the $D_v(R)$ distribution functions[31,32] and the lines correspond to the log–normal distributions. The average particle diameters, d_{SAXS}, were calculated from the $D_v(R)$ distribution functions.

8.3 nm for 50GT-4, 1GT-4, T-4, and 1GT-24, respectively. Despite 7–12% smaller than the average particle size measured by SAXS, they follow the same trend.

3.3 GO functional groups

The FTIR spectra of GO, TiO_2 and their composites are depicted in Fig. 5. The spectrum of the sample T-4 shows a broad peak below 750 cm^{-1} corresponding to Ti–O–Ti bonding and two peaks at 1630 and 1385 cm^{-1}, which can be attributed to O–H vibration and Ti–O stretching modes, respectively.[4] The starting GO sample shows a more complex spectrum, owing to various types of oxygen functional groups: C=O stretching (carbonyl) around 1731 cm^{-1}, water –OH bending and –OH (hydroxyl) at 1618 cm^{-1}, C–O–H (carboxyl) at 1384 cm^{-1}, C–O (epoxy) at 1224 cm^{-1}, –OH stretching (phenolic) at 1170 cm^{-1}, C–O stretching (hydroxyl) at 1051 cm^{-1}, C–H (aromatic) at 856 cm^{-1}.[4,42] These vibration modes are also observed for the sample 50GT-4, but with a lower intensity, as expected due to the lower concentration of GO in the sample. Degradation of the GO functional groups during synthesis is also possible, as discussed later. Moreover, the appearance of the broad peak around 400–750 cm^{-1} suggests that both Ti–O–Ti and Ti–O–C bonding are present in this sample. Indeed, Ti–O–C can be formed by condensation of the hydroxyl group of TiO_2 and functional groups of GO.[43] The spectra of the two composites with 1 wt% GO loading, namely 1GT-4 and 1GT-24, do not show the characteristic GO peaks, due to the low amount of GO. On the contrary, these samples show only the vibration modes observed for TiO_2. Nevertheless, a broad band at 400–750 cm^{-1} (Ti–O–Ti and Ti–O–C) is also observed for these two samples.

The Raman spectra of starting GO and the nanocomposite samples are depicted in Fig. 6. They show the characteristic D (sp^3 carbon) and G (sp^2 carbon) band of graphene oxide at about 1350 and 1600 cm^{-1}, respectively.[13,44] The presence of both bands in 1GT-4 and 1GT-24 indicates the existence of graphene oxide in both samples. The G band is assigned to the in-plane vibrations of the graphene network, whereas the D band is due to out of plane vibrations attributed to the presence of structural defects. The intensity ratio of D and G bands (I_D/I_G) of 50GT-4, 1GT-4 and 1GT-24 are 0.98, 1.06 and 1.09, respectively. These values are higher than that measured for the starting GO (0.92). An increased I_D/I_G ratio has been typically observed after GO reduction, which could be attributed to the decrease in the average size of the sp^2 domains in the 2D carbon network.[13,25,45] Therefore, this implies a partial reduction and an increase in defects after attachment with TiO_2 nanoparticles.

The partial reduction of GO during synthesis is confirmed by the XPS C1s spectra in Fig. 7(a). Peak deconvolution for the pure GO sample allows to distinguish the graphitic sp^2 carbon atoms with binding energy at around 284.6 eV and the two types of oxidized carbon atoms C–O and C=O (or O–C=O) with binding energy at 286.5 and 287.7 eV, respectively.[46] The peak deconvolution for the spectra of 50GT-4, 1GT-4, and 1GT-24, shows the existence of carbon with different oxidation states in all the nanocomposite materials. The partial reduction of graphene oxide was confirmed by calculating the area ratios of the peak corresponding to the oxidized carbon over the peak of the fully reduced carbon atoms: A_{C-O}/A_{C-C} and $A_{O-C=O}/A_{C-C}$.[4] The results are reported in Table 1. The A_{C-O}/A_{C-C} and $A_{O-C=O}/A_{C-C}$ values of all the GO–TiO_2 nanocomposites are about 50% lower than those of the starting GO, meaning that a half of the oxygen-containing groups on GO was removed after decoration with TiO_2 and heating at 100 °C. In addition, the synthesis time (4 hours or 24 hours) appears to have no influence on the GO

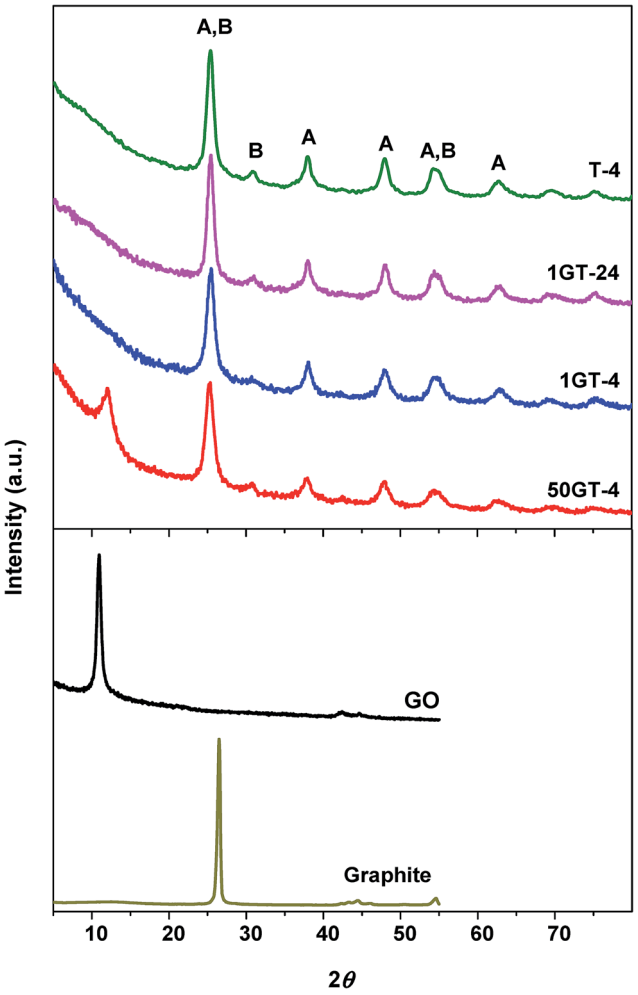

Fig. 4 XRD patterns of GO, starting graphite, TiO_2 (T-4), and GO–TiO_2 nanocomposites (1GT-4, 1GT-24 and 50GT-4). A and B indicate the characteristic peaks of anatase and brookite phases, respectively.

reduction. Moreover, the binding energy of the peak corresponding to most oxidized carbon atoms shift from 287.7 eV for the pure GO sample to 289.3 eV for the two TiO_2 powders containing the 1 wt% GO, thus suggesting by the formation of coordination structure in these materials,[17,47] *i.e.* the formation of Ti–O–C moieties. This shift is less pronounced for 50GT-4 (binding energy = 287.9 eV), as a consequence of the formation of GO nanoribbons and the lower exposure of the GO functional groups to the interaction with TiO_2 nanoparticles.

In Fig. 7(b), the Ti2p spectra of all the samples show two main peaks around 459.2 and 464.9 eV, with a splitting energy of 5.7 eV, assigned to $Ti2p_{1/2}$ and $Ti2p_{3/2}$ spin–orbital splitting photoelectrons of Ti^{4+}, respectively.[25,48] As expected for GO–TiO_2 nanocomposites prepared under mild conditions, these spectra exclude the presence of Ti–C bonds, since there are no deconvoluted peaks at around 466.0 and 460.3 eV.[49]

The 3 fitted peaks of O1s show in Fig. 7(c). The OC=O and C=O, C–OH and CO–H of GO are at 530.9, 532.5 and 533.9 eV, respectively.[50] The pure TiO_2 shows characteristic Ti–O–Ti peak at 529.8 eV and the surface Ti–OH bond at 530.5 eV.[50] The peaks

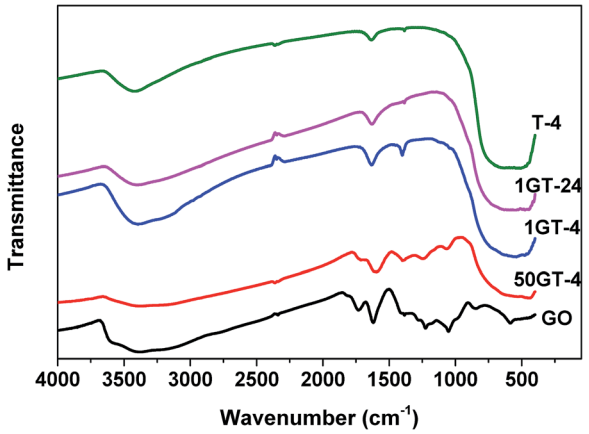

Fig. 5 FTIR transmittance spectra of the starting GO powder (black line), the pure TiO_2 reference (green line), and of the GO–TiO_2 nanocomposites 50GT-4 (red line), 1GT-4 (blue line) and 1GT-24 (pink line).

at around 530.5, 532.2 and 533.5 eV are assigned to Ti–O–C,[51] O–C, and –OH vibration modes,[25,50] respectively, indicating the existence of the Ti–O–C linkage in the TiO_2–GO nanocomposites. This is an important feature since Ti–O–C linkage may promote the electron transfer from the TiO_2 nanoparticles to graphene structures during photocatalytic applications,[25] and impact their mutual evolution during synthesis and thermal annealing.

3.4 Synthesis temperature

By considering the morphology of GO–TiO_2 nanocomposites with different compositions (see above), we investigate the effect of the synthesis temperature on the structural evolution during annealing of the nanocomposite with 50 wt% GO loading and the pure TiO_2 reference. Fig. 8(a) shows the XRD patterns of the pristine TiO_2 references (T-4) prepared at 60 °C and 100 °C, and the 50GT samples synthetizes at a temperature ranging from 60 °C to 100 °C. All 50GT-4 nanocomposites

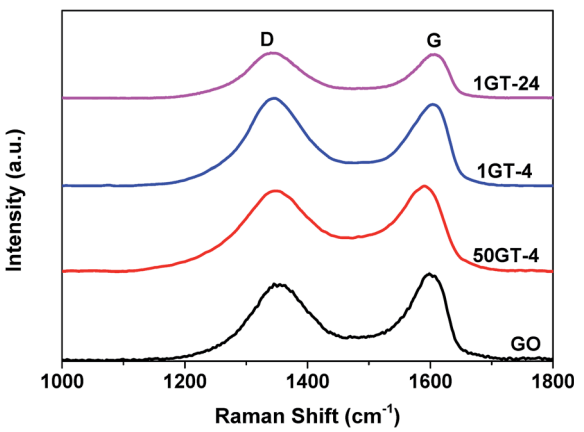

Fig. 6 Raman spectra of GO and GO–TiO_2 composites from 100–1800 cm^{-1}; D and G band corresponding to sp^3 and sp^2 carbon, respectively.

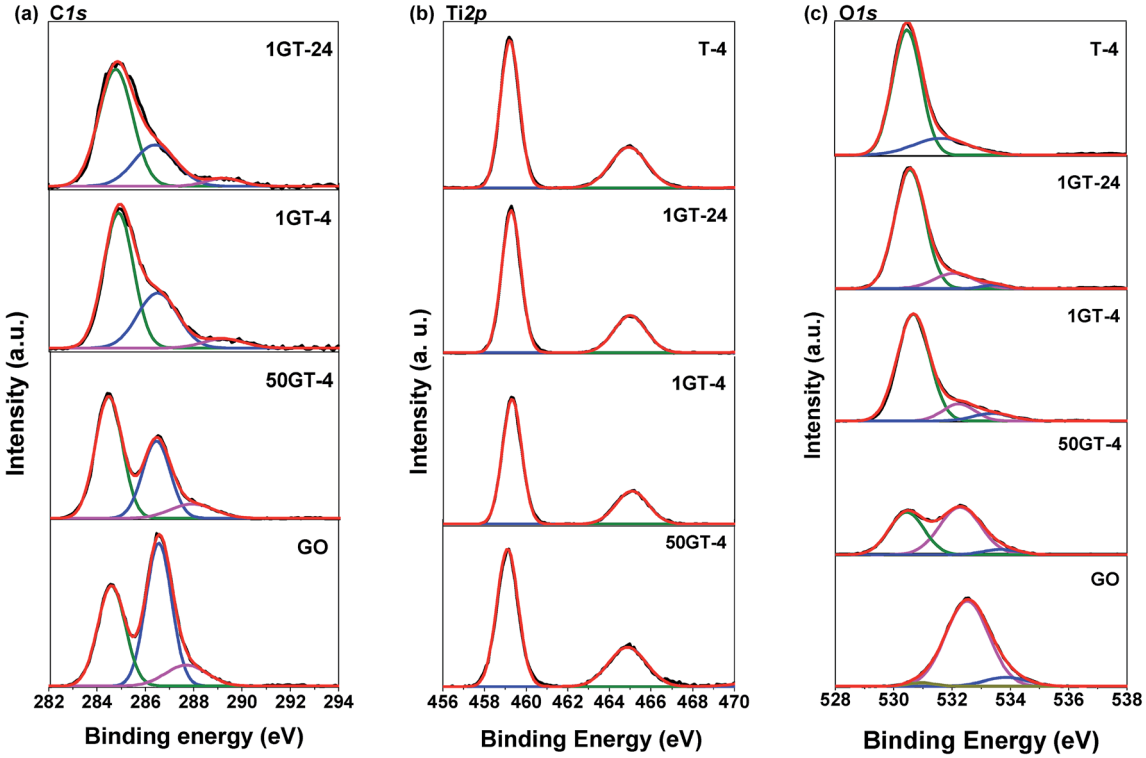

Fig. 7 XPS spectra of GO, T-4, and GO–TiO_2 composites: (a) C1s spectra, (b) Ti2p spectra, and (c) O1s spectra.

exhibit the characteristic GO peak, which allows for calculating the interlayer distance and the average thickness of the GO nanoribbons in the composite materials by using the Bragg law and the Scherrer equation, respectively. Fig. 8(b) shows that the interlayer distance for GO sheets in the samples prepared between 60 °C and 80 °C is 8.1 Å. This distance is close to that measured for the pristine GO powder (8.4 Å), but larger than the value of 7.36 Å measured for the composite prepared at 100 °C. Thus, the decrease of the interlayer distance results in thinner GO ribbons.

The samples synthetized at 60 °C appear to consist of amorphous TiO_2 (both T-4 and 50GT-4), as shows in Fig. 8(a). The main phase, anatase, is present from 70 °C, while the presence of brookite is observed in the sample synthetized at 80 °C. Under these conditions (pH ~ 6 and synthesis temperature > 70 °C), the formation of both phases has already been reported in literature.[52–54] Titania characteristic peaks were used to calculate the size of anatase crystals and their fraction in the total crystalline phase. Nevertheless, we observe that the fraction of anatase phase, calculated as described in the Experimental section, increases with the temperature. Indeed, both pure TiO_2 and GO–TiO_2 composites prepared at 100 °C contain slightly more than 70% of anatase phase, while for the 50GT-4 sample prepared at 80 °C the fraction of anatase phase was calculated to be around 65%. The presence of GO in the reaction mixture has a significant role in influencing the size and agglomeration of the TiO_2 nanoparticles, but it does not affect the anatase/brookite ratio. As expected, the average size of anatase crystallites increases with the temperature, *e.g.*, from 4.1 nm for the 50GT sample prepared at 60 °C to 6.4 nm for the one prepared at 100 °C.

Table 1 XPS peak area ratio (A_{C-O}/A_{C-C} and $A_{O-C=O}/A_{C-C}$) of GO, 50GT-4, 1GT-4 and 1GT-24

Sample name	A_{C-O}/A_{C-C}	$A_{O-C=O}/A_{C-C}$
GO	1.34	0.41
50GT-4	0.65	0.26
1GT-4	0.54	0.27
1GT-24	0.44	0.28

3.5 Thermal annealing

The mass loss during annealing of TiO_2 and 50GT-4 synthetized at various temperatures is analyzed and the curves are shown in Fig. 9(a). As typical of GO-based materials, TG curves show three main steps of mass change. The mass loss of GO and the composites below 150 °C is due to the evaporation of physisorbed and nanoconfined water.[55] The major loss of the mass is due to the degradation of the functional groups on graphene oxide at 150–350 °C: (i) H_2O release through the dehydration of the neighboring hydroxyl groups and (ii) releasing of CO and CO_2 from the decarbonation reaction.[55] The last step, above 350 °C, has been assigned to the carbon network degradation[25,56] and to the removal of the most stable oxygen functionalities.[57] The mass loss of TiO_2 synthetized in 4 hours at 60 °C and 100 °C is depicted in Fig. 9(b). Also in this case, physisorbed water evaporates below 150 °C.[58] As expected, above this temperature there are only little changes in

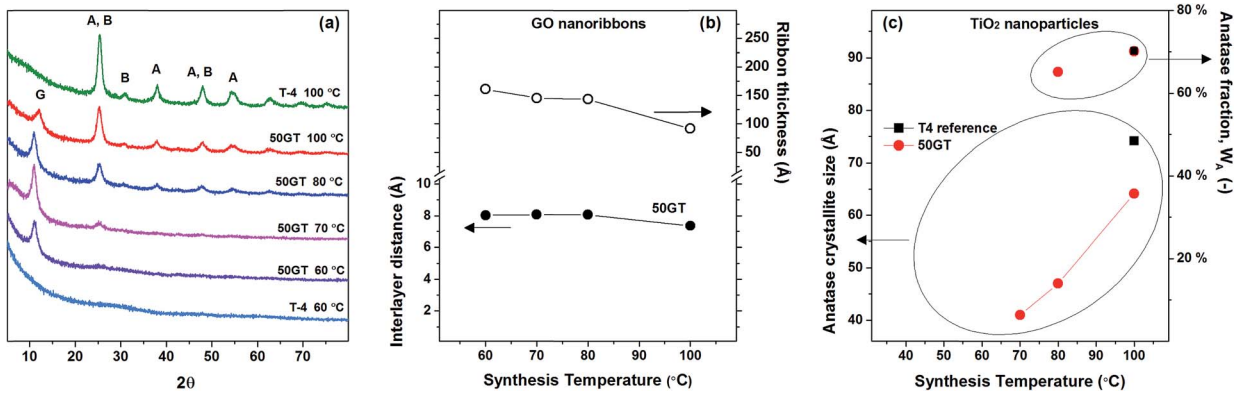

Fig. 8 (a) XRD patterns of 50GT and T-4 synthetized in 4 hours at a temperature between 60 °C and 100 °C. The letter "G" indicates the peak characteristic of graphene oxide. "A" and "B" indicate the characteristic peaks of anatase and brookite phases, respectively. (b) The characteristic peak of graphene oxide was used to calculate the distance between GO sheets (Bragg) and the average thickness of the GO nanoribbons (Scherrer) in the nanocomposites. (c) The characteristic peaks of TiO_2 were used to calculate the size of the anatase crystallites (Scherrer) and the anatase fraction, W_A (eqn (3) in the Experimental section).

chemical composition,[54] and mass loss is not observed toward until 800 °C. The data in Fig. 9(a) and (b) were used to calculate the theoretical mass loss of a 50 : 50 w/w physical mixture of graphene oxide–TiO_2 and the results are compared with the TG analysis of the 50TG samples in Fig. 9(c). In the 150–350 °C range, the mass loss of the composites is lower than that of a physical mixture of graphene oxide and TiO_2. This is again a strong indication of chemical bonding between GO and TiO_2,[25] *i.e.* the condensation of oxygen functional groups on GO and hydroxyl groups on titania particles to form Ti–O–C.[1]

The DSC results in Fig. 10(a) show the exothermic transitions of GO, TiO_2 and their composites (50GT 60 °C, 50GT 70 °C, 50GT 80 °C and 50GT 100 °C). The pure GO powder shows the typical exothermic sharp peak with onset temperature ($T_{GO,ons}$) at 149 °C and minimum temperature ($T_{GO,min}$) at 187 °C, which is due to the reduction reaction of the oxygen functional groups.[59] The 50GT composites also display the characteristic peak, but surprisingly their $T_{GO,ons}$ and $T_{GO,min}$ shift toward higher temperatures (Table 2). The difference in reduction onset temperature, $\Delta T_{GO,ons}$, is plotted as a function of the synthesis temperature in Fig. 10(b). The highest $\Delta T_{GO,ons}$ value, namely 49.9 °C, is observed for the sample prepared at 60 °C. $\Delta T_{GO,ons}$ drops down to ~32 °C with increasing the synthesis temperature for the 50GT powders prepared at 80 °C and 100 °C. This is again an indication of the chemical interaction between GO and TiO_2. GO rearrangement in the more stable and ordered reduced structure is hindered by the fact that TiO_2 nanoparticles are chemically anchored over the surface of the thin GO ribbons.[27] The shift of $T_{GO,ons}$ from 149 °C of starting GO to over 180 °C in the composite samples suggests that titanium dioxide can retard the degradation of the functional groups on graphene oxide, because the condensation reaction between moieties on graphene oxide and titanium dioxide leads to stabilization of oxygen functional groups.[1] The 50GT samples prepared at lower temperatures are highly amorphous and have small particle size. Therefore, they possess a high surface area and high defect density to interact with GO.

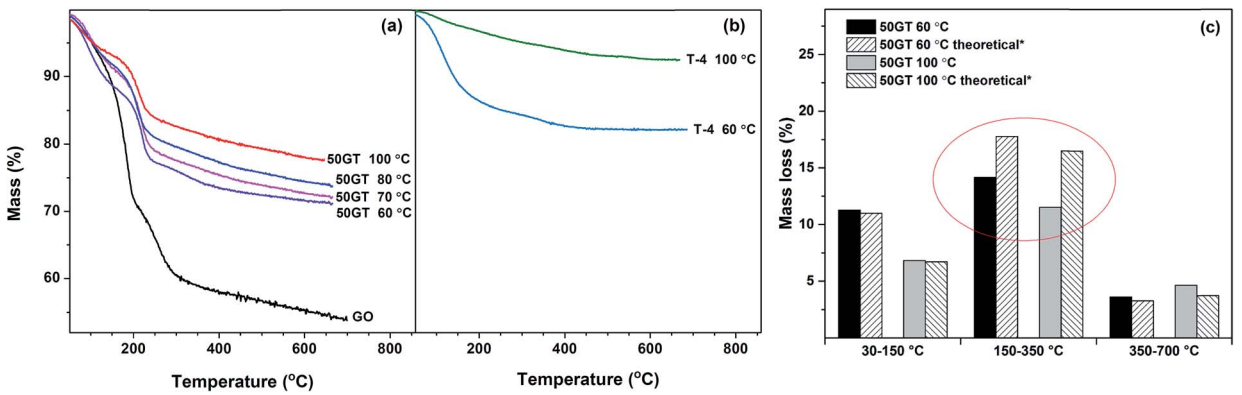

Fig. 9 (a) Thermogravimetric curves of GO and GO–TiO_2 nanocomposites (50GT 60 °C, 50GT 70 °C, 50GT 80 °C, and 50GT 100 °C); (b) pure titanium dioxide (T-4) synthetized at 60 °C and 100 °C; (c) TG data were used to calculate the mass loss in a theoretical physical mixture 50 : 50 GO : TiO_2 and the results were compared with the mass loss of the real 50GT samples. The red cycle stresses the difference between the theoretical mixture and the real sample in the temperature range between 150 and 350 °C.

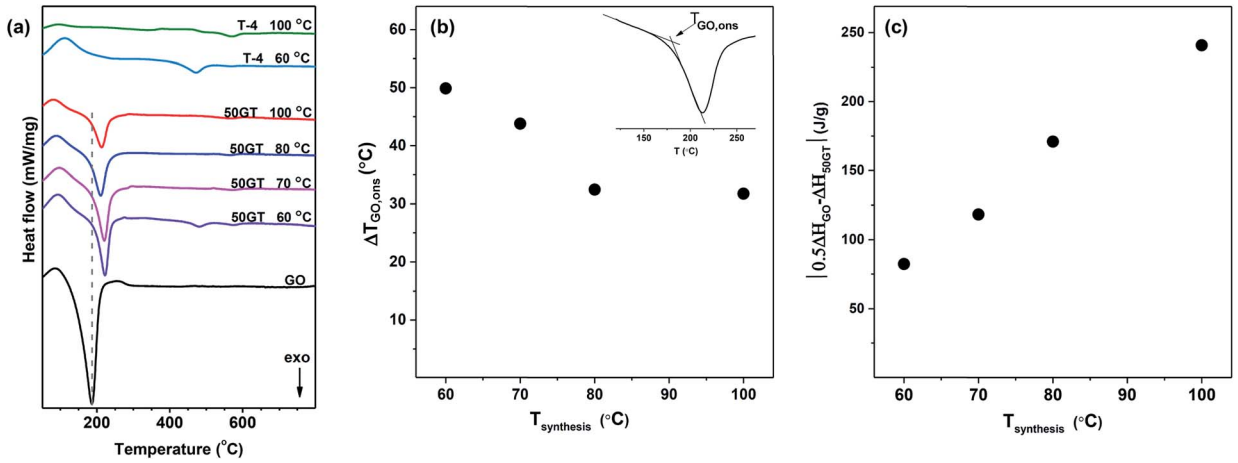

Fig. 10 (a) DSC curves of GO, 50GT and T-4 prepared at a temperature between 60 °C and 100 °C. (b) The difference between the reduction onset temperature ($\Delta T_{GO,ons}$) of the 50GT samples and the starting GO as a function of the synthesis temperature. (c) The difference of the reduction enthalpy ($|0.5\Delta H_{GO} - \Delta H_{50GT}|$) between the theoretical physical mixture containing 50% GO ($0.5\Delta H_{GO}$) and 50GT samples (ΔH_{50GT}) as a function of the synthesis temperature.

Table 2 Characteristics of the GO reduction peak for the starting GO powder and the TiO_2 nanocomposites with 50 wt% GO loading synthetized in 4 hours at a temperature between 60 °C and 100 °C: peak onset temperature ($T_{GO,ons}$), peak minimum ($T_{GO,min}$) and GO reduction enthalpy (ΔH) as calculated from the peak area

Sample name	$T_{GO,ons}$ (°C)	$T_{GO,min}$ (°C)	ΔH (J g^{-1}) at 180–220 °C
50GT 100 °C	180.9	213.1	−299.6
50GT 80 °C	181.6	193.1	−369.4
50GT 70 °C	192.9	220.7	−422.1
50GT 60 °C	199.0	222.2	−458.2
GO	149.1	186.7	−1081.0

The peak areas in Fig. 10(a) clearly indicate that the synthesis temperature has an impact also on the enthalpy associated with the reduction of GO. Indeed, the reduction enthalpy values reported in Table 2 clearly show that enthalpy decreases with the reaction temperature. Therefore, the difference between reduction enthalpy of the 50GT composite (ΔH_{50GT}) and the theoretical reduction enthalpy of a physical mixture containing 50 wt% GO ($0.5\Delta H_{GO}$) is plotted as a function of the synthesis temperature in Fig. 10(c). The different trend can be attributed to the fact that the TiO_2 nanocrystals present in the sample prepared at high temperature disrupt the order of the reduced graphitic structure.[60]

Fig. 11 shows the differential scanning calorimetry curves in the temperature range of 350–650 °C of 50GT and T-4 synthetized for 4 hours between 60 °C and 100 °C. The peaks for both the amorphous TiO_2-to-anatase and the anatase-to-rutile transformations can be observed at around 470 °C and 570 °C in T-4 60 °C, respectively.[61] In contrast, T-4 100 °C shows a transformation peak of anatase to rutile at 570 °C.[50] The behavior of 50GT 60 °C at 400–650 °C is alike the one of T-4 60 °C. However, the anatase formation from amorphous phase of 50GT 60 °C occurs at a temperature about 10 °C higher

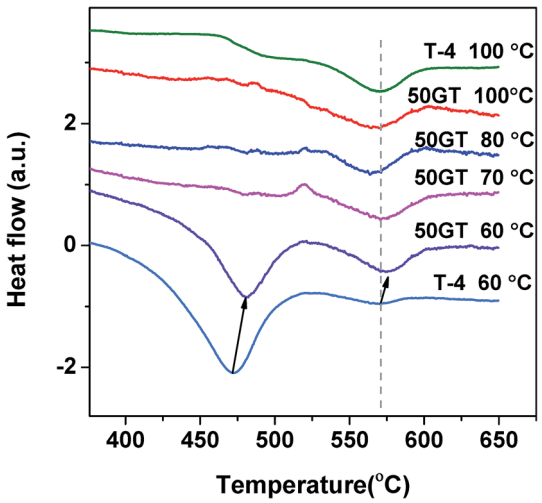

Fig. 11 Differential scanning calorimetry (DSC) curves of TiO_2 transitions at 350–650 °C for the samples 50GT (synthesis temperature between 60 and 100 °C) and T-4 (synthesis temperature 60 and 100 °C).

than that of T-4 60 °C. On the contrary, the calorimetric scansions of the composites synthesized at 70–100 °C show only a weak hump at 570 °C for the anatase-to-rutile transition.

4. Conclusions

In this work, we study the structural evolution of GO–TiO_2 composites during synthesis and thermal annealing. We have found experimental evidence for the interface chemical bonding between TiO_2 nanoparticles and GO, even when a simple synthetic method is used under mild conditions, namely at pH 6 and at temperature between 60 °C and 100 °C. Using this method, the anatase–brookite mixed phase has been obtained, which is dispersed on GO monolayers for a low amount of GO (1 wt%), but decorates GO nanoribbons for

a high amount of GO (50 wt%). TEM analysis shows facets of TiO_2 nanocrystals laying on the GO nanoribbon, thus suggesting a strong interaction between the two materials. FTIR and XPS analyses suggest the formation of Ti–O–C interactions. The Ti2p XPS spectra exclude the formation of a significant number of Ti–C bonds, but the interaction between GO and TiO_2 is strong enough to induce mutual shaping during synthesis and the thermal evolution.

The role of GO on TiO_2 morphology is summarized as follows: (i) GO affects TiO_2 particle size and dispersion, since GO prevents agglomeration. However, GO does not influence type of phase or phase fraction of TiO_2. (ii) GO retards the thermal transition from amorphous TiO_2 to anatase phase.

The presence of TiO_2 nanoparticles influences the GO morphology as follows: (i) TiO_2 nanoparticles intercalate GO sheets, depending on the GO/TiO_2 ratio. It is possible to obtain GO nanoribbons or isolated GO sheet. (ii) When GO nanoribbons are decorated with TiO_2 nanoparticle, their thermal reduction occurs at a higher temperature than the pure GO powder.

Thus, this work gives new insights into the mutual shaping of TiO_2 and GO during sol–gel synthesis and thermal annealing, and hence, enables rational design of new photocatalysts with desired morphology and performances.

Conflicts of interest

There are no conflicts to declare.

Acknowledgements

The authors gratefully acknowledge financial support from the Thai Ministry of Science and Technology and the European Union project H2020-MSCA-RISE-2014, no. 645551. Fondazione San Paolo and Turin University are acknowledged for funding the project Microbusters (Progetto d'Ateneo 2014).

References

1 L. M. Pastrana-Martínez, S. Morales-Torres, V. Likodimos, J. L. Figueiredo, J. L. Faria, P. Falaras and A. M. T. Silva, *Appl. Catal., B*, 2012, **123–124**, 241–256.
2 N. Zhang, M.-Q. Yang, S. Liu, Y. Sun and Y.-J. Xu, *Chem. Rev.*, 2015, **115**, 10307–10377.
3 R. Sadri, K. Z. Kamali, M. Hosseini, N. Zubir, S. N. Kazi, G. Ahmadi, M. Dahari, N. M. Huang and A. M. Golsheikh, *J. Dispersion Sci. Technol.*, 2017, **38**, 1302–1310.
4 L. Zhang, Q. Zhang, H. Xie, J. Guo, H. Lyu, Y. Li, Z. Sun, H. Wang and Z. Guo, *Appl. Catal., B*, 2017, **201**, 470–478.
5 R. K. Upadhyay, N. Soin and S. S. Roy, *RSC Adv.*, 2013, **4**, 3823–3851.
6 M. Faraldos and A. Bahamonde, *Catal. Today*, 2017, **285**, 13–28.
7 Y. Jiang, W.-N. Wang, D. Liu, Y. Nie, W. Li, J. Wu, F. Zhang, P. Biswas and J. D. Fortner, *Environ. Sci. Technol.*, 2015, **49**, 6846–6854.
8 J. Xu, J. Tian, Y. Zhang, A. Riaz, Y. Liu, M. Zhi, Z. Hong and C. Zhou, *RSC Adv.*, 2016, **6**, 40304–40311.
9 O. Ola and M. M. Maroto-Valer, *J. Photochem. Photobiol., C*, 2015, **24**, 16–42.
10 M. Ge, C. Cao, J. Huang, S. Li, Z. Chen, K.-Q. Zhang, S. S. Al-Deyab and Y. Lai, *J. Mater. Chem. A*, 2016, **4**, 6772–6801.
11 J. Jing, Y. Zhang, W. Li and W. W. Yu, *J. Catal.*, 2014, **316**, 174–181.
12 Y. Liu, *RSC Adv.*, 2014, **4**, 36040–36045.
13 S. Stankovich, D. A. Dikin, R. D. Piner, K. A. Kohlhaas, A. Kleinhammes, Y. Jia, Y. Wu, S. T. Nguyen and R. S. Ruoff, *Carbon*, 2007, **45**, 1558–1565.
14 M. Sohail, H. Xue, Q. Jiao, H. Li, K. Khan, S. Wang and Y. Zhao, *Mater. Res. Bull.*, 2017, **90**, 125–130.
15 X. Yang, X. Jiang, Y. Huang, Z. Guo and L. Shao, *ACS Appl. Mater. Interfaces*, 2017, **9**, 5590–5599.
16 X. Cheng, S. Ding, J. Guo, C. Zhang, Z. Guo and L. Shao, *J. Membr. Sci.*, 2017, **536**, 19–27.
17 Y. Min, K. Zhang, W. Zhao, F. Zheng, Y. Chen and Y. Zhang, *Chem. Eng. J.*, 2012, **193–194**, 203–210.
18 L.-L. Tan, S.-P. Chai and A. R. Mohamed, *ChemSusChem*, 2012, **5**, 1868–1882.
19 C. Hu, T. Lu, F. Chen and R. Zhang, *J. Chin. Adv. Mater. Soc.*, 2013, **1**, 21–39.
20 Q. Zhang, Y. He, X. Chen, D. Hu, L. Li, T. Yin and L. Ji, *Chin. Sci. Bull.*, 2011, **56**, 331–339.
21 C. Xu, Y. Xu and J. Zhu, *ACS Appl. Mater. Interfaces*, 2014, **6**, 16117–16123.
22 C. P. Athanasekou, N. G. Moustakas, S. Morales-Torres, L. M. Pastrana-Martínez, J. L. Figueiredo, J. L. Faria, A. M. T. Silva, J. M. Dona-Rodriguez, G. E. Romanos and P. Falaras, *Appl. Catal., B*, 2015, **178**, 12–19.
23 X.-F. Sun, J. Qin, P.-F. Xia, B.-B. Guo, C.-M. Yang, C. Song and S.-G. Wang, *Chem. Eng. J.*, 2015, **281**, 53–59.
24 L. M. Pastrana-Martínez, S. Morales-Torres, J. L. Figueiredo, J. L. Faria and A. M. T. Silva, *Water Res.*, 2015, **77**, 179–190.
25 M. Nawaz, W. Miran, J. Jang and D. S. Lee, *Appl. Catal., B*, 2017, **203**, 85–95.
26 B. Petrie, R. Barden and B. Kasprzyk-Hordern, *Water Res.*, 2015, **72**, 3–27.
27 T. N. Lambert, C. A. Chavez, B. Hernandez-Sanchez, P. Lu, N. S. Bell, A. Ambrosini, T. Friedman, T. J. Boyle, D. R. Wheeler and D. L. Huber, *J. Phys. Chem. C*, 2009, **113**, 19812–19823.
28 V. Boffa, D. G. Perrone, G. Magnacca and E. Montoneri, *Ceram. Int.*, 2014, **40**, 12161–12169.
29 V. Boffa, H. Etmimi, P. E. Mallon, H. Z. Tao, G. Magnacca and Y. Z. Yue, *Carbon*, 2017, **118**, 458–466.
30 W.-N. Wang, Y. Jiang and P. Biswas, *J. Phys. Chem. Lett.*, 2012, **3**, 3228–3233.
31 O. Glatter, *J. Appl. Crystallogr.*, 1980, **13**, 7–11.
32 P. V. Konarev, M. V. Petoukhov, V. V. Volkov and D. I. Svergun, *J. Appl. Crystallogr.*, 2006, **39**, 277–286.
33 H. Zhang and J. F. Banfield, *J. Phys. Chem. B*, 2000, **104**, 3481–3487.
34 X. Zhang, P. Suresh Kumar, V. Aravindan, H. H. Liu, J. Sundaramurthy, S. G. Mhaisalkar, H. M. Duong,

S. Ramakrishna and S. Madhavi, *J. Phys. Chem. C*, 2012, **116**, 14780–14788.
35 B. E. Warren and P. Bodenstein, *Acta Crystallogr.*, 1966, **20**, 602–605.
36 H. Ünlü, N. J. M. Horing and J. Dabowski, *Low-Dimensional and Nanostructured Materials and Devices: Properties, Synthesis, Characterization, Modelling and Applications*, Springer, 2015.
37 J. Wang, X. Gao, Y. Wang and C. Gao, *RSC Adv.*, 2014, **4**, 57476–57482.
38 K. Gigant, A. Rammal and M. Henry, *J. Am. Chem. Soc.*, 2001, **123**, 11632–11637.
39 M. Azarang, A. Shuhaimi and M. Sookhakian, *RSC Adv.*, 2015, **5**, 53117–53128.
40 M. Azarang, A. Shuhaimi, R. Yousefi and S. P. Jahromi, *RSC Adv.*, 2015, **5**, 21888–21896.
41 G. Jiang, Z. Lin, C. Chen, L. Zhu, Q. Chang, N. Wang, W. Wei and H. Tang, *Carbon*, 2011, **49**, 2693–2701.
42 M. Safarpour, A. Khataee and V. Vatanpour, *Ind. Eng. Chem. Res.*, 2014, **53**, 13370–13382.
43 T.-D. Nguyen-Phan, V. H. Pham, E. W. Shin, H.-D. Pham, S. Kim, J. S. Chung, E. J. Kim and S. H. Hur, *Chem. Eng. J.*, 2011, **170**, 226–232.
44 X. Pan, Y. Zhao, S. Liu, C. L. Korzeniewski, S. Wang and Z. Fan, *ACS Appl. Mater. Interfaces*, 2012, **4**, 3944–3950.
45 W. Wang, J. Yu, Q. Xiang and B. Cheng, *Appl. Catal., B*, 2012, **119–120**, 109–116.
46 J. Zhang, Z. Xiong and X. S. Zhao, *J. Mater. Chem.*, 2011, **21**, 3634–3640.
47 D. Peng, W. Qin, X. Wu, J. Wu and Y. Pan, *RSC Adv.*, 2015, **5**, 77138–77146.
48 O. Akhavan and E. Ghaderi, *J. Phys. Chem. C*, 2009, **113**, 20214–20220.
49 M. S. A. Sher Shah, A. R. Park, K. Zhang, J. H. Park and P. J. Yoo, *ACS Appl. Mater. Interfaces*, 2012, **4**, 3893–3901.
50 B. Chen, J. Sha, W. Li, F. He, E. Liu, C. Shi, C. He, J. Li and N. Zhao, *ACS Appl. Mater. Interfaces*, 2016, **8**, 2495–2504.
51 W.-S. Wang, D.-H. Wang, W.-G. Qu, L.-Q. Lu and A.-W. Xu, *J. Phys. Chem. C*, 2012, **116**, 19893–19901.
52 B. K. Mutuma, G. N. Shao, W. D. Kim and H. T. Kim, *J. Colloid Interface Sci.*, 2015, **442**, 1–7.
53 H. Cheng, J. Ma, Z. Zhao and L. Qi, *Chem. Mater.*, 1995, **7**, 663–671.
54 Y. Hu, H.-L. Tsai and C.-L. Huang, *J. Eur. Ceram. Soc.*, 2003, **23**, 691–696.
55 W. Zhang, Y. Li and S. Peng, *ACS Appl. Mater. Interfaces*, 2016, **8**, 15187–15195.
56 W. L. Zhang and H. J. Choi, *Chem. Commun.*, 2011, **47**, 12286–12288.
57 J. I. Paredes, S. Villar-Rodil, A. Martínez-Alonso and J. M. D. Tascón, *Langmuir*, 2008, **24**, 10560–10564.
58 M. E. Simonsen and E. G. Søgaard, *J. Sol-Gel Sci. Technol.*, 2010, **53**, 485–497.
59 Z. Ji, G. Zhu, X. Shen, H. Zhou, C. Wu and M. Wang, *New J. Chem.*, 2012, **36**, 1774–1780.
60 Z. Gohari Bajestani, A. Yürüm and Y. Yürüm, *RSC Adv.*, 2016, **6**, 32831–32838.
61 P. J. Huang, H. Chang, C. T. Yeh and C. W. Tsai, *Thermochim. Acta*, 1997, **297**, 85–92.